International Journal of Applied Earth Observation and Geoinformation 122 (2023) 103417

Contents lists available at ScienceDirect

International Journal of Applied Earth Observation and Geoinformation

journal homepage: www.elsevier.com/locate/jag

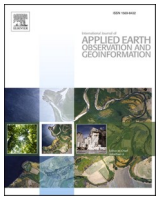

# Mapping depth-integrated microphytobenthic biomass on an estuarine tidal flat using Sentinel satellite data

Ting Zhang [a,b], Bo Tian [a,*], Yujue Wang [a], Dongyan Liu [a], Yunxuan Zhou [a], Daphne van der Wal [b,c,*]

[a] State Key Laboratory of Estuarine and Coastal Research, East China Normal University, 200062 Shanghai, China
[b] NIOZ Royal Netherlands Institute for Sea Research, Department of Estuarine and Delta Systems, P.O. Box 4400 AC, Yerseke, The Netherlands
[c] Faculty of Geo-Information Science and Earth Observation (ITC), University of Twente, P.O. Box 217, 7500 AE Enschede, The Netherlands

ARTICLE INFO

*Keywords:*
Biomass estimation
Sentinel satellite data
Microphytobenthos
Sediment grain-size
Vertical distribution
Tidal flat

ABSTRACT

Microphytobenthos (MPB) are central to benthic tidal flat ecological networks. Large-scale information on total MPB biomass is difficult to obtain from traditional in-situ measurements. Here, we assessed the effectiveness of using surface sediment properties as proxies for predicting the total (depth-integrated) MPB biomass with Sentinel satellite data. First, the best subset regression was applied to the in-situ data to determine the properties that best predict the biomass decay rate with depth (sampling every cm up to 10 cm depth). Then, data from a controlled laboratory experiment were used to analyse the spectral response to different sediment properties (i.e., variations in sediment grain size, organic matter and water content). Subsequently, an algorithm was developed to obtain the spatial distribution of the sediment properties and the depth-integrated total MPB biomass from remote sensing data. Finally, we presented a case study in which the seasonal dynamics of total (depth-integrated) MPB biomass were obtained from Sentinel-2 Multispectral Instrument (MSI) satellite data using the Google Earth Engine (GEE) platform. The results showed that (1) the vertical distribution of MPB biomass on a tidal flat could be predicted by the surface MPB biomass, median grain-size ($D_{50}$) and water content ($W_0$) of the sediment (top 1 cm); (2) the near infrared (NIR) band absorption depth was a key feature in estimating $D_{50}$ and $W_0$; and (3) the seasonal variation in the total (depth-integrated) MPB biomass was prominent in Chongming Dongtan, Changjiang Estuary. We concluded that the depth-integrated exponential decay algorithm was useful for estimating total MPB biomass and, combined with mappable sediment-surface data, could help map the total MPB biomass in estuarine tidal flats at a large scale.

## 1. Introduction

Tidal flats are crucial in the estuarine food web, supporting birds, fish and shellfish (Kromkamp et al., 2006). Although the global distribution and trajectory of tidal flats have been preliminarily mapped and the amount of tidal flat area has been quantified (Murray et al., 2019), the quality of tidal flats has still not been effectively assessed. Microphytobenthos (MPB) consist of unicellular eukaryotic algae and cyanobacteria (MacIntyre et al., 1996), represent food for macrofauna, particularly deposit feeders and suspension feeders (Miller et al., 1996), and can be used as a good proxy for the quality of tidal flats. MPB primary production can be over 50% of the total ecosystem carbon fixation, comparable to phytoplankton (Underwood and Kromkamp, 1999), and MPB production amounts to approximately 0.5 Gt C/yr globally (Cahoon, 1999). MPB also contribute to the stabilisation of the sediment, as they produce sticky extracellular polymeric substances (EPS) (Kim et al., 2021; Paterson and Hagerthey, 2001). Thus, MPB play a role in providing ecosystem services through multiple pathways (Hope et al., 2020).

As calculating MPB biomass from cell abundance is inefficient (MacIntyre et al., 1996), the photosynthetic pigment chlorophyll *a* (Chl-a) is used as an index of MPB biomass in most cases (e.g., Daggers et al., 2018; Méléder et al., 2003a). MPB biomass has high spatial (horizontal) variability, ranging from the microscale (<1 m) to the mesoscale (1–300 m) (Benyoucef et al., 2014; Kromkamp et al., 2020), resulting from different abiotic and biotic factors. Desiccation, light, temperature,

* Corresponding authors at: NIOZ Royal Netherlands Institute for Sea Research, Department of Estuarine and Delta Systems, P.O. Box 4400 AC, Yerseke, The Netherlands (D. van der Wal). State Key Laboratory of Estuarine and Coastal Research, East China Normal University, 200062, Shanghai, China (B. Tian).
*E-mail addresses:* btian@sklec.ecnu.edu.cn (B. Tian), daphne.van.der.wal@nioz.nl (D. van der Wal).

https://doi.org/10.1016/j.jag.2023.103417
Received 19 September 2022; Received in revised form 28 April 2023; Accepted 5 July 2023
Available online 11 July 2023

sediment resuspension rates, water content, salinity, sediment composition, tidal height, and intertidal elevation are the primary abiotic factors that affect the distribution of MPB (Benyoucef et al., 2014; Coelho et al., 2009; Daggers et al., 2020b; Serôdio et al., 2006). Additionally, grazing and bioturbation by macrofauna (van der Wal et al., 2008) contribute to the variability of MPB. Moreover, anthropogenic activities, such as (shellfish) fisheries (Méléder et al., 2003b;Echappé et al., 2018; Méléder et al., 2003b), and dredging and engineering works (de Vet et al., 2017) may have a direct or indirect effect (e.g., via sedimentation/erosion) on the variability of MPB. Monitoring of MPB can help us to better understand the response of MPB to different environmental variables and to optimize coastal management.

MPB biomass also varies with depth. Frankenbach et al. (2019) distinguished three functional layers of MPB: i) an upper 'canopy' of photosynthetically active cells, usually in the uppermost 0.6 to 0.8 mm of the sediment (Lichtenberg et al., 2020), ii) a 'cell reserve' that can replace these cells through vertical migration within a few hours, usually within the top mms of the sediment (Jesus et al., 2006), with the depth depending on species (e.g., motile diatoms can cover a vertical distance of approximately 3.2 mm in one low tide event) and iii) 'backup' cells that serve as a carbon sink under the 'cell reserve' layer. To the best of our knowledge, although many studies have examined the deeper layers using in situ data (Middelburg et al., 2000; Riaux-Gobin et al., 1987; Riekenberg et al., 2020), most studies focus on the MPB within the superficial zone for the study of metabolism, primary production, circadian rhythm, etc., including the 'canopy' layer and 'cell reserve' layer, using field/laboratory measurements and/or remote sensing techniques (Barillé et al., 2007; Kromkamp et al., 2020; Méléder et al., 2020; Murphy et al., 2008). The vertical distribution of MPB may also be affected by bioturbation by benthic macrofauna, disturbing the sediment (Montserrat et al., 2009, 2008), and by resuspension. An accurate estimation of the total MPB biomass across all functional layers, including both the horizontal (spatial) and vertical (depth) distribution, is necessary.

Through traditional field measurements, an aboveground biomass/belowground ratio for the MPB vertical distribution at a 10 cm depth can be obtained on tidal flats. For example, Frankenbach et al.(2019) found that the surface biomass (0–0.5 cm) accounted for one-fifth to one-third of the total biomass at 0–10 cm depth, while Yin et al. (2016) suggested that the top 1 cm contributed up to 60% of the whole sediment core at 0–10 cm. Compared with laborious field sampling, modelling can integrate measured data and estimate the total biomass across all three functional layers. Brotas and Serôdio (1995) proposed a simple model describing the depth distribution of biomass for different intertidal sediments in the superficial zone, which was further developed by Frankenbach et al.(2019). In this model, except for the surface MPB biomass ($C_0$), the variation in biomass with depth is described by a decay term related to the burial rate, named the depth-constant decay rate (kc). As a parameter related to depth, kc is considered to depend on the MPB biomass and sediment composition (i.e., sediment grain-size). Previous studies have shown that due to the reduced sediment resuspension and slower burial of MPB, sites with a high surface MPB biomass had greater decline in MPB with depth (Liu et al., 2013); and sites with a high mud content also had a higher MPB biomass at the surface and a stronger exponential decline rate than sandier sites (Du et al., 2010). Hence, applying a model and constructing an algorithm of the kc based on the sediment properties may help to estimate the total (i.e. depth-integrated) MPB biomass at large spatial horizontal scales from the mesoscale (1–300 m) to macroscale (>300 m).

Satellite observations allow monitoring of the tidal flat surface globally, complementing in situ sampling and laboratory experiments. Remote sensing has been used to retrieve surface MPB biomass, with a spectral resolution ranging from multispectral to hyperspectral and a spatial resolution ranging from metres to kilometres (above mesoscale), using Aqua MODIS (van der Wal et al., 2010), SPOT (Méléder et al., 2003b), Landsat (Daggers et al., 2018), Sentinel-2 (Daggers et al., 2020a; Haro et al., 2022 ), airborne hyperspectral data (Combe et al., 2005; Kazemipour et al., 2012), etc. Despite these advancements, little attention is given to retrieve the vertical distribution of MPB biomass in the functional layers using remote sensing. Remote sensing has been used to study the sediment background effect in examining MPB (Barillé et al., 2011; Kazemipour et al., 2012; Launeau et al., 2018), finding that spectral reflectance varied with sediment water content, grain size, and organic matter. Therefore, remote sensing may support spatial estimates of kc-related sedimentary physicochemical properties by building related algorithms, helping to estimate total MPB biomass.

This study will focus on the estimation of total MPB biomass, including both the surface and subsurface biomass. The specific objectives of this study are 1) to develop a model to quantify the MPB vertical distribution (biomass decay rate at depths>1 cm) based on in situ MPB biomass depth profile data and other sediment characteristics (i.e., sediment temperature, salinity, water content, grain size, and organic matter); 2) to conduct a controlled experiment to investigate the spectral reflectance response to different sediment properties (i.e., water content, sediment grain size and organic matter), select the spectral features that best estimate the biomass decay rate, and integrate this information into an algorithm to retrieve total biomass; and 3) to apply the algorithm to Sentinel satellite imagery, providing seasonal maps of total MPB biomass.

## 2. Materials and methods

### 2.1. Experimental site

Chongming Dongtan (31.25°–31.38°N, 121.50°–122.05°E) is located on Chongming Island, the largest island in the mouth of the Chanjiang Estuary in eastern China (Fig. 1). It has 24,155 ha of estuarine wetlands with a subtropical monsoon climate, which are composed of mudflats dominated by MPB (i.e., diatoms) and salt marshes dominated by *Phragmites australis*, *Scirpus mariqueter* and *Spartina alterniflora*. The area is an international Ramsar site (since 1998) and a national nature reserve (since 2005). A *Spartina* control and bird habitat optimisation project started in 2013, in which a cofferdam was constructed in the northern part of the study area to remove *Spartina* by immersion. The cofferdam with the inlet was abandoned after the completion of the project.

### 2.2. Overview of methodology

Fig. 2 displays the framework for total MPB biomass mapping. It includes six main stages, including (i) in-situ data collection, (ii) laboratory analysis, (iii) satellite remote sensing data processing, (iv) construction of the MPB biomass decay rate algorithm, (v) construction of the surface variables algorithm and (vi) total MPB biomass mapping. The five stages are detailed in the following subsections.

### 2.3. Data collection and processing

#### 2.3.1. In-situ data collection

Three seasonal field campaigns were conducted between June 2019 and December 2020 (Fig. 1). Spectral data were obtained by an ASD HandHeld 2 field portable spectroradiometer (HH2 325–1075, USA) at low tides under clear sky conditions, with measurements at most sites from 10:00 to 13:30 (China Standard Time, CST) at 40 cm standard height, which covers a field of view of ca. 0.025 $m^2$. The in-situ spectra were resampled to match the spectral resolution of the S2 data using the spectral response function (SRF) (ESA, 2015) for further use. Synchronous measurements of the sediment surface temperature (using an Oxidation Reduction Potential metre, Kedida CT-8022, with 0.1 °C resolution) and salinity (using a salinity pen, AZ-8371, with 0.10 resolution) were conducted after spectral measurement (see Zhang et al. (2021) for a detailed description).

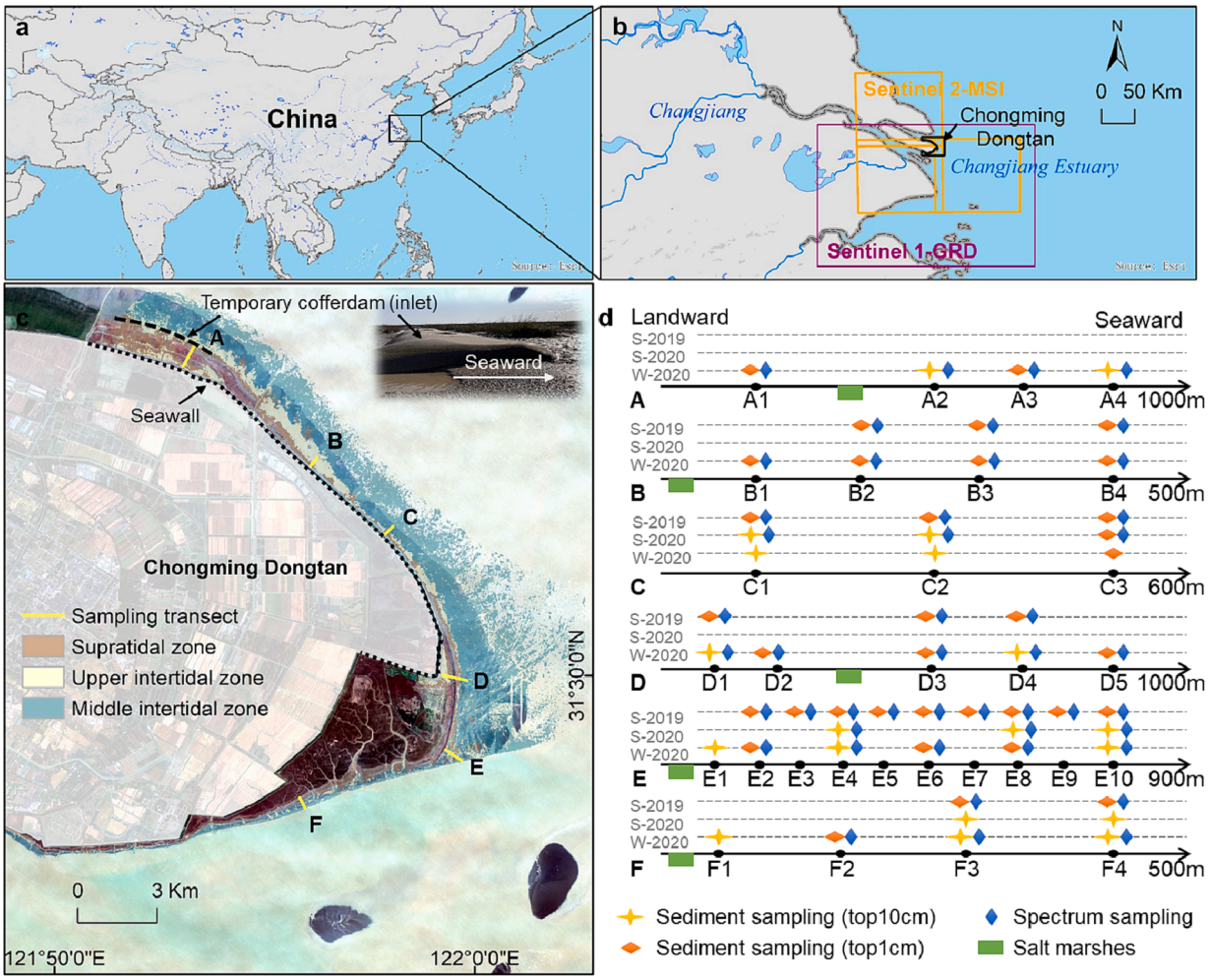


**Fig. 1.** Study area and sample point distribution. (a) Location of the Changjiang Estuary; (b) location of the study area, Chongming Dongtan, and the different satellite sensor footprints (Sentinel-2 Multispectral Instrument (MSI) in orange, Sentinel-1 synthetic aperture radar (SAR) Ground Range Detected (GRD) in purple); (c) sampling transects in the study area, including transects A, B, C, D, E and F; (d) specific sampling points collected in summer (S) and winter (W) of 2019 and 2020. Note that not all transects were sampled in all periods (see main text for sampling strategy). (For interpretation of the references to colour in this figure legend, the reader is referred to the web version of this article.)

The sediment was then collected on six transects, with three replicate samples obtained at one station. There is a dynamic adjustment of sampling strategy according to the sampling target (and other factors, such as winter sampling in 2019 was cancelled due to Covid-19), which can be divided into the following four parts. First, to determine the vertical distribution of MPB, we collected three individual replicates of 10 cm depth sediment cores at 19 sites in summer 2020 and winter 2020 (Fig. 1) using a syringe (3 cm diameter) with a cut nozzle, and then we sectioned the cores into 1 cm slices using a blade. Second, we collected a number of samples of the upper 1 cm, mainly for the construction of remote sensing algorithms of the surface parameters (n = 35, see Fig. 1). Considering the potential impact of human activities (the cofferdam in the northern area), we added transect A in the winter of 2020. Third, based on the data results from summer 2019, three groups of surface sediment, each with a different level of median grain size ($D_{50}$), were collected at sites C1, E8, and E10 (weight ca. 50–80 g) in summer 2020 for the indoor spectrum experiment. It is also why only three transects were covered in the summer of 2020. Finally, we collected an independent dataset on August 23, 2020, to validate the accuracy of the surface parameters algorithm. Each sampling site was relatively homogeneous, and all samples were placed in an icebox and transported to the laboratory for further analysis.

### 2.3.2. Laboratory analysis

Laboratory analysis included the measurement of sediment properties and the spectral response under controlled conditions. Using wet samples, Chl-a was measured through extraction in 90% acetone in 24 h at − 4 °C and determination using the acidification method and a fluorometer (Trilogy Laboratory Fluorometer 7200–000) (Strickland and Parsons, 1972). We measured three times for each replicate sample. The MPB biomass was expressed as the Chl-a per unit area of sediment over the operationally defined sediment depth of 1 cm. The gravimetric water content W was obtained after freeze-drying and expressed as the water mass on a dry-mass basis (Lambe and Whitman, 1991), calculated by the formula:

$$W(\%) = \frac{weight\ \ wet\ \ sediment(g) - weight\ \ dry\ \ sediment(g)}{weight\ \ dry\ \ sediment(g)} \times 100$$

The median sediment grain size $D_{50}$ was measured by a laser particle size analyser (LS13 320, USA) via laser diffraction. Additional sediment samples were analysed for total organic carbon (TOC) by an elemental analyser (Vario EL III, Germany). More detailed information can be found in Zhang et al.(2021).

Then, an indoor spectrum measurement experiment was designed to quantify the spectral response under controlled $D_{50}$, water content and TOC levels. Following the results from Ming-Yi et al.(1993), we placed

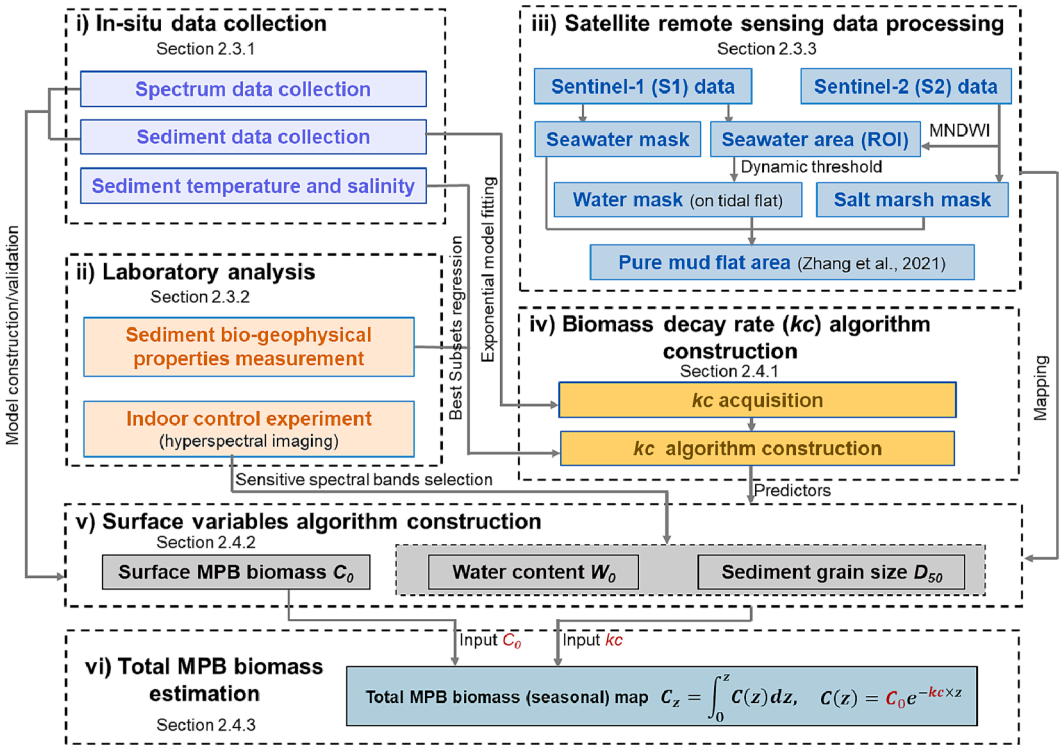


**Fig. 2.** Framework for total microphytobenthos (MPB) biomass mapping: i) In-situ data collection; ii) Laboratory analysis; iii) Satellite remote sensing data processing; iv) Biomass decay rate algorithm construction; v) The surface variables algorithm construction; and vi) Total MPB biomass algorithm construction and mapping. MNDWI means modified normalized difference water index; kc means the biomass decay rate; $C_0$ means surface MPB biomass; and $C_z$ means total MPB biomass at depth z.

the three abovementioned sediment groups at room temperatures (ca. 20 °C) for at least one month for the natural degradation of Chl-a. After determining the $D_{50}$ (9.04 μm, 52.25 μm, and 119.87 μm, in the three groups) and TOC (0.07%, 0.18%, and 0.76%) of the freeze-dried samples, we divided these samples into two parts (i.e., six groups) and removed the organic matter from one of them using a high-temperature burning method (muffle furnace, at 550 °C for 5 h). We then placed these samples (10 g) into matte black vessels (inner diameter: 5.50 cm) on a 0.0001 balance and injected 0 g, 1 g, 2 g, 3 g, 4 g, 5 g, and 7 g of water (i.e., 7 classes of water content), in turn, with a syringe to control the water content, stirring quickly, to conduct the spectral measurement. Using high-intensity stabilized broadband line light and a standard hyperspectral camera (Pika XC2, Resonon, USA, spectral resolution of 1.3 nm, ranging from 400 nm to 1000 nm), we obtained a hyperspectral image for each sample after calibrating the imager for both dark current (objective lens blocked) and reflectance reference. For specific settings,

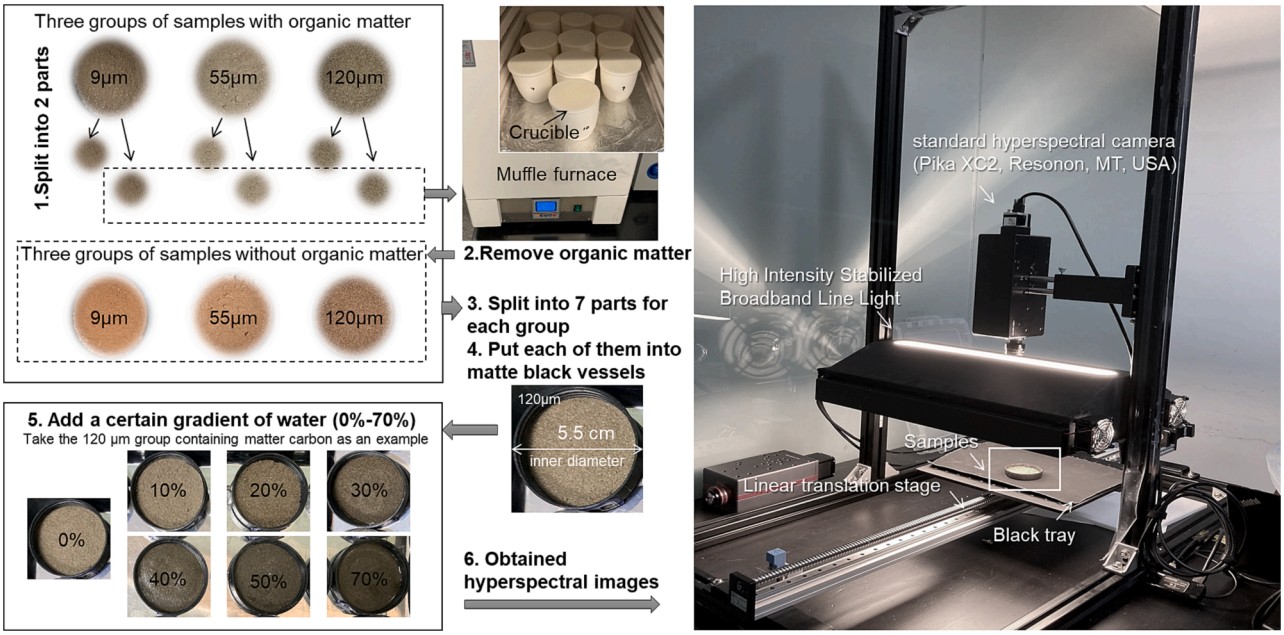


**Fig. 3.** Schematic diagram of the indoor experimental setup.

see Fig. 3. Using SpectrononPro software, we extracted the average brightness of the hyperspectral images and obtained the reflectance data of the samples according to the reference data of the white board, which had a ~ 99% brightness. Then, we calculated the rate of change (ROC) of reflectance with increasing water content and increasing $D_{50}$ to determine the sensitive band using

$$ROC = \frac{n\sum_{i=1}^{n}(i \times Ref_i) - (\sum_{i=1}^{n} i \times \sum_{i=1}^{n} Ref_i)}{n\sum_{i=1}^{n} i^2 - (\sum_{i=1}^{n} i)^2}$$

where n is the total number of spectral curves, Ref is reflectance and i is the i-th reflectance.

### 2.3.3. Sentinel dataset acquisition and processing

We used two primary sources of satellite image data, including Copernicus Sentinel-1 SAR (S1) images (spatial resolution of 10 m) and Copernicus Sentinel-2 MSI (S2) optical images (spatial resolution of 10 to 60 m) collected from March 2020 to February 2021. Data acquisition and processing were completed through Google Earth Engine (GEE). S1 (ImageCollection: 'COPERNICUS/S1_GRD') data were used to distinguish land and seawater areas by masking seawater based on Otsu's method (Otsu, 1979). Otsu's method is a thresholding algorithm that can realize the binarisation of greyscale images by automatically determining the optimal segmentation threshold. To mask the ponding water area on the tidal flat, we chose the region of interest (ROI) from the seawater areas in the S2 images to calculate the modified normalized difference water index (MNDWI) (Xu, 2006), an index based on the green and shortwave infrared light. Due to the high concentrations and temporal variability of suspended sediments in the water of the Changjiang estuary, we used the mean value of MNDWI in the ROI as a dynamic threshold for each S2 image to mask the water area on the tidal flat, following the methods outlined in Zhang et al.(2021).

For the S2 images, we used atmospherically corrected reflectance data (from ImageCollection: 'COPERNICUS/S2_SR' in GEE). To further remove cloud pixels, we filtered them for the whole year using the property fields CLOUDY_PIXEL_PERCENTAGE, retained images with a cloudiness of less than 65%, and masked the pixels using the property field S2_CLOUD_PROBABILITY (from ImageCollection: 'COPERNICUS/S2_CLOUD_PROBABILITY' in GEE, 10 m resolution), leaving pixels with values of less than 30%. S2 data with fewer than 15 reference points were discarded, which left 46 images for the whole year range from March 2020 to February 2021 (spring: 14 images, summer: 8 images, autumn: 8 images, winter: 16 images). To best compare the images in season, we normalised for these selected images following the methods in Daggers et al. (2020a). Specifically, we used a set of reference points (n = 40, including stable points in high or low reflectance on land that is not affected by the tide, see Fig. S2 and Table S1) and applied an empirical line calibration to each image by regressing to the surface reflectance of an atmospherically corrected image with clear sky (image of May 29, 2021). In addition, pixels with salt marshes were masked using a red-edge band-based (Sentinel 2, band 5) algorithm; a detailed description can be found in Zhang et al. (2021). A S2 image collected on August 23, 2020, 10:25:49.024 (CST), was used for validation.

## 2.4. Algorithm development and mapping

### 2.4.1. Building the algorithm to estimate the biomass decay rate

After obtaining the in situ MPB biomass for all the 10 cm depth core samples, the decay rate kc was obtained by fitting a simple negative exponential model using Origin 2021b software. The content of subsurface living cells may be considered low at a very large depth and can only surface through intense sediment resuspension and mixing (Frankenbach et al., 2019). Here, we set the value as 0.01 mg Chl-a·$m^{-2}$ at 100 cm. Thus, following the formulation by Brotas and Serôdio (1995), the decay rate was calculated as follows:

$$C_z = C_0 e^{-kc \times z} \quad (1)$$

where $C_z$ and $C_0$ are the MPB biomass at a depth z and the surface (z = 0), respectively, and kc is the decay rate of MPB biomass with depth.

To test whether the surface environmental parameters are better than the average value at 0–10 cm depth for modelling kc, we used redundancy analysis (RDA) with CANOCO software to compare the correlation between these parameters and kc. All the environmental parameters were normalised to remove dimensional differences. The angles among the variables in RDA plots typically denote the degree of correlation between the individual variables, and the smaller the angle is, the more significant the correlation is. Then, using the best subset linear regression method (R package, function regsubsets), we obtained the best predictors and prediction model of kc from the sediment variables measured at the surface, including the biomass ($C_0$), $D_{50}$, water content ($W_0$), sediment temperature ($T_0$), salinity ($S_0$) and TOC ($O_0$) of the sediment and their interaction factors (i.e., $C_0$:$D_{50}$ means $C_0$, $D_{50}$ and $C_0 \times D_{50}$). We selected regression models (by exhaustive search, forward and backward stepwise, and sequential replacement of parameters, respectively), limited to 5 predictors to avoid overfitting. Due to limited in-situ data (n = 19), the model performance was further evaluated using the leave-one-out (LOO) cross-validation method (Moore and Lee, 1994) with the performance represented by the coefficient of determination ($R^2$). The model with the lowest Bayesian information criterion (BIC) (Schwarz, 1978) was selected as the best prediction model for kc.

### 2.4.2. Building the algorithm to estimate the surface variables

After establishing the kc regression model using the in-situ sediment data, we analysed the in-situ spectral data collected from both summer and winter to build the algorithm of the surface variables $C_0$, $D_{50}$ and $W_0$, which are predictors of kc. After resampling the in-situ spectral data to the spectral resolution of S2 data using ENVI 5.3 software, these data were used to extract the red band absorption depth and construct regression models to estimate $C_0$, the model with a lower BIC was selected for mapping.

For $D_{50}$ and $W_0$, we first used the resampled spectral data from the indoor controlled experiments to determine the sensitive spectral band, then used this band in resampled in-situ spectral data to construct regression models and selected the model with higher $R^2$ and lower AIC for mapping. Among them, two selectable bands in the near-infrared wavelength are sensitive to $D_{50}$ and $W_0$, i.e. bands 8 and 8A. Because band 8 has higher spatial resolution and covers more near-infrared wavelengths, we selected band 8 as the input parameter for algorithm construction.

### 2.4.3. Total biomass estimation

Eq. (2) provides an expression for quantifying the total MPB biomass. With the estimated values of $C_0$ and kc, the MPB total biomass $C_{(z=100cm)}$ was then calculated using the following integral operation.

$$C_z = \int_0^z C(z)dz \quad (2)$$

where Cz is the MPB biomass at any depth z, and its calculation is shown in Eq. (1). Here, z is 100 (cm). Therefore, the total MPB biomass was expressed as a concentration (Chl-a per unit area of sediment), and the value was calculated over an operationally defined sediment depth of 100 cm.

To obtain the spatiotemporal dynamics, we mapped the seasonal variation in total MPB biomass by constructing mean seasonal composites using the data collected from March 2020 to February 2021. According to the algorithm described above, we directly obtained $C_0$, $D_{50}$, $W_0$, kc, and total biomass from S2 data in GEE. We validated these surface parameters using the independent database obtained on August 23, 2020.

## 3. Results

### 3.1. In-situ data analysis and decay rate algorithm development

From the averaged in-situ data per site (n = 19, see Tables S2 for the detail value), we found that the MPB biomass decreased with depth following a negative exponential decay rate, which fit well with Eq. (1) ($R^2 = 0.74 \pm 0.18$, $p < 0.01$, n = 19). The average kc was 0.24 ± 0.21 $cm^{-1}$, ranging from 0.02 to 0.69 $cm^{-1}$. The contribution of the surface MPB biomass (0–1 cm depth) to the total MPB biomass (1–10 cm depth) was 25.45 ± 14.55%, ranging from 11.47% to 59.76%. Fig. 4 shows examples of the single replicate sample data, demonstrating the range of the in-situ measured top 10 cm vertical profiles of MPB biomass under different kc, $C_0$, $D_{50}$, $W_0$, and TOC ($O_0$) values and the total biomass at the top 10 cm ($C_{10}$).

RDA between the kc and environmental parameters (i.e., MPB biomass; water content; median grain size; temperature; salinity; and TOC) showed that the surface values correlate more with kc than did the average values at a 0–10 cm depth (comparison of angles in Fig. S3). This finding suggested a potential of mapping kc using surface parameters. Moreover, although there was a significant correlation between $C_0$, $D_{50}$, $W_0$, and $O_0$ ($p < 0.01$), there were only two significant positive partial correlations, i.e., between $C_0$ and kc ($r = 0.789$, $p = 0.001$), and between $D_{50}$ and kc ($r = 0.597$, $p = 0.024$), while there were no significant partial correlations between kc and any other parameter (see Supplementary Table S6). The best subset regression analysis showed that the best predictors for kc estimation were $C_0$, $D_{50}$, and the interaction of $D_{50}$ and $W_0$, which had lower BIC and LOO error values than any other model (see Tables S3 and S4).

### 3.2. Surface parameter algorithm development and evaluation

The indoor spectrum experiment showed that a higher $W_0$ and $D_{50}$ corresponded to a lower reflectance in the visible and near-infrared range (400–1000 nm). For $W_0$ levels up to 40%, the reflectance rate slowly decreased with increasing $W_0$. For $W_0$ levels up to 70% (i.e., $D_{50}$ = 120 μm, brown-yellow dotted line in Fig. 5), the reflectance at 980 nm was lower than that at 800 nm. In addition, a lower TOC corresponded with a higher reflectance in the blue and green bands and a lower reflectance in the red and NIR bands (Fig. 5). Fig. 6 shows the ROC of reflectance with change in $D_{50}$ and $W_0$ under non-controlled and controlled TOC conditions (for samples with TOC: $O_0 \neq 0\%$, and for samples without TOC: $O_0 = 0\%$). In Fig. 6a and c, we found that the NIR bands were sensitive to $D_{50}$ under different $W_0$ conditions with or without TOC content, especially under unsaturated conditions, i.e., $W_0 < 40\%$. Similarly, Fig. 6b and d show that NIR bands were sensitive to $W_0$ under different $D_{50}$ values with or without TOC content.

The best subset regression analysis results showed that apart from $C_0$, $D_{50}$ and $W_0$ were the critical factors for kc estimation (Tables S3 and S4), and the indoor spectrum experiment showed that NIR was the sensitive spectral channel for estimating $D_{50}$ and $W_0$. Therefore, we used the NIR absorption depth to build a regression algorithm for $D_{50}$ and $W_0$.

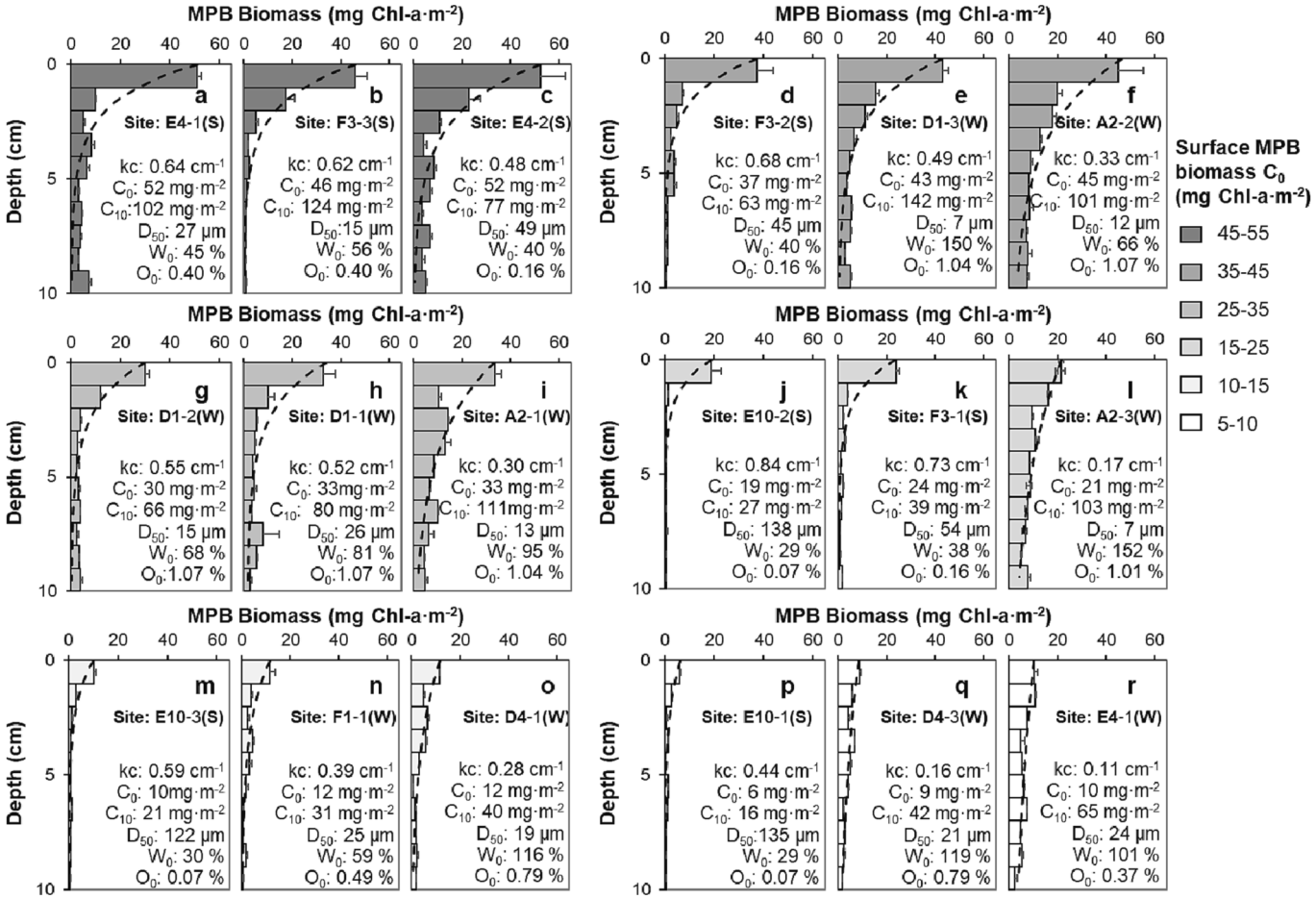


**Fig. 4.** Examples of the vertical distribution of microphytobenthos (MPB) biomass. Data of the six group are displayed based on different surface MPB biomasses ($C_0$), ranging from approximately 55 mg Chl-a·$m^{-2}$ to 5 mg Chl-a·$m^{-2}$. The dashed line is a fitting line obtained according to Eq. (1). Each vertical profile data point is collected from a single replicate sample at the same or different sites in summer (S) or winter (W). Kc is the biomass decay rate; $C_{10}$ is the total biomass between 0 and 10 cm depth; $D_{50}$ is the surface median grain-size; $W_0$ is the surface water content; and $O_0$ is the surface sediment TOC. See Fig. 1 for locations. The colour ranges from dark grey to white with decreasing $C_0$.

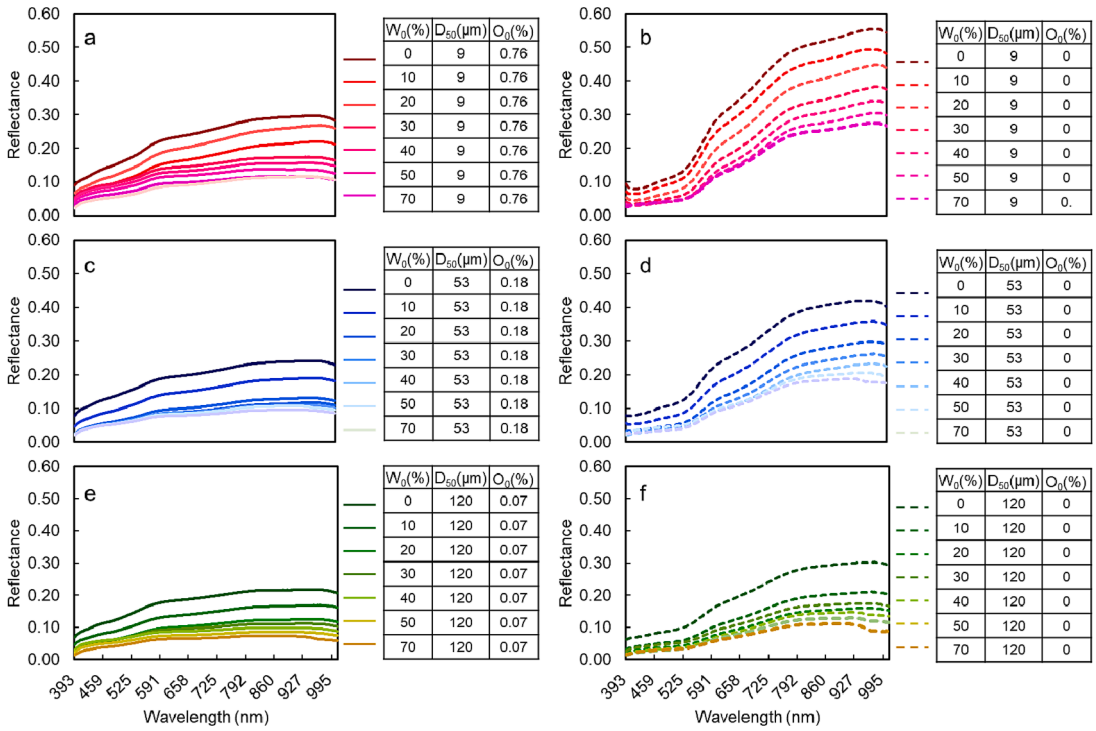


**Fig. 5.** Six groups of original spectral reflectances measured in the indoor experiment, with different sediment grain size $D_{50}$ (ranging from 9 μm to 120 μm), different water contents $W_0$ (ranging from 0% to 70%) and different total organic carbon TOC (ranging from 0% to 0.76%).

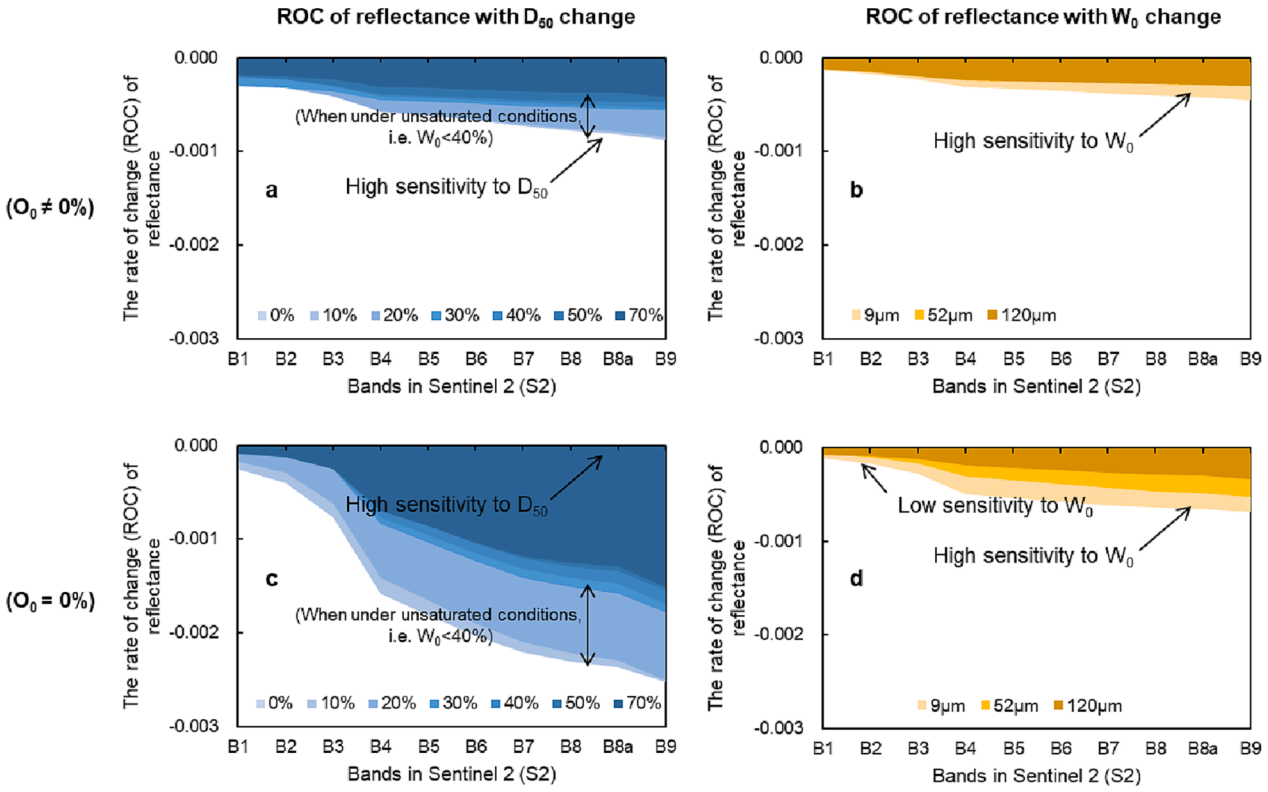


**Fig. 6.** The rate of change (ROC) of reflectances with change in sediment grain size D50 (a, c) and water content W0 (b, d) based on the spectral data obtained from indoor experiments: a and b include the influence of organic matter ($O_0 \neq 0\%$), and c and d exclude the influence of organic matter ($O_0 = 0\%$). The blue gradients denote different levels of water content, whereas the orange/brown colours denote different sediment grain sizes (see legend). (For interpretation of the references to colour in this figure legend, the reader is referred to the web version of this article.)

Considering that the sediment was water-saturated in the field, and that the effect of both water content and grain size on the continuum values is nonlinear (Verpoorter et al., 2014), we chose the exponential regression model (two-parameter exponential function $y = ae^{bx}$ (Ratkowsky, 1990)) to build the algorithm, which had better performance (lower BIC value) than the linear models (Tables S5). For the estimation of $C_0$, the linear red absorption depth-based regression model was selected after the performance compared with the exponential model. Fig. 7 shows the regression model of $D_{50}$, $W_0$ and $C_0$, built based on the in-situ data collected from different seasons. See Fig. S1 for the calculation method of absorption depth used in this study, following van der Meer (2004).

### 3.3. Satellite-based MPB total (depth-integrated) biomass mapping

Maps of the surface MPB biomass $C_0$, as well as $D_{50}$, $W_0$ and the decay rate retrieved from satellite data formed the basis for the maps of total MPB biomass (Fig. 8). Fig. S4 shows the validation results of surface parameters using an independent database collected on August 23, 2020. The determination coefficients $R^2$ for $C_0$, $D_{50}$, and $W_0$ were $R^2 = 0.70$ ($n = 33$, $p < 0.01$), $R^2 = 0.59$ ($n = 33$, $p < 0.01$) and $R^2 = 0.31$ ($n = 33$, $p < 0.01$), respectively.

Satellite-retrieved total MPB biomass $C_{total}$ (Fig. 8) has achieved a high level in summer, at 111.0 ± 23.2 mg Chl-a·m$^{-2}$ and is also high in autumn, at 106.6 ± 17.9 mg Chl-a·m$^{-2}$. Moreover, there are also high values in summer for $C_0$ and kc, reaching 23.6 ± 6.3 mg Chl-a·m$^{-2}$ and 0.38 ± 0.23 cm$^{-1}$, respectively. In contrast, $D_{50}$ showed an opposite trend, reaching a minimum in summer (17.9 ± 18.0 μm). Variability in $W_0$ for the whole area is higher in summer (80.2 ± 44.9%), but the mean value is higher in autumn, reaching 92.4 ± 26.9%.

The annual cycle for $C_{total}$ (and $C_0$) spatially varied with a north–south differentiation. The rapid growth of total biomass in the narrow southern area mainly occurred in summer. In the northern area, the rapid growth of the lower tidal flat (seaside) mainly occurred in spring and summer, while that in the upper tidal flat mainly occurred in autumn (Fig. 8). In general, the northern region, with its higher water content and smaller sediment grain size, has a higher total biomass than do the southern areas. The spatiotemporal variation pattern of $W_0$ was consistent with that of $C_{total}$.

## 4. Discussion

Intertidal total (depth-integrated) MPB biomass plays a significant role in the functioning of estuarine tidal flat ecosystems. A remote sensing regression-based model was developed to estimate the total MPB biomass across all three functional layers and its seasonal spatiotemporal variation. The potential drivers for the variation in the total MPB biomass and the applicability of the method are discussed below.

### 4.1. Potential drivers of the total biomass variation

Chongming Dongtan is part of the rapidly seaward growing area of the Changjiang Estuary delta (Zhang et al., 2018). MPB biomass varies spatially and temporally, with relevance for high-trophic level organisms such as macrobenthos and migratory shorebirds. The results showed that the total MPB biomass had an apparent north–south differentiation, and had the highest value in summer and was also high in autumn. The following factors may drive this spatial–temporal variation. First, flood currents in the Changjiang Estuary carry a large amount of sediment, ranging from 0.7 to 2,068 mg of suspended particulate matter l$^{-1}$ (Wei et al., 2021). These currents deflect northwards due to the Coriolis effect, which can cause scour on the southeast coast of Dongtan (Li et al., 2014) and accretion in the north. In addition, the size of suspended sediments in the dry season (winter) was found to be larger than that in the flood season (summer), and a high flow velocity of spring tides can entrain coarser sediments to tidal flats (Wang et al., 2020). This may be used to explain the lower MPB biomass in the northernmost area in winter, which has an abandoned cofferdam (Fig. 1). Even though there is an opening for the tide to enter and exit, it slows the current, impedes the regular exchange of sediments, and prevents the deposition of sediment.

Second, the dominant MPB species, which have specific environmental preferences, differ on the north and south sides. Sediment salinity varies significantly between the north and south sides of the study area, with higher levels in the north and lower levels in the south. Early studies found that different MPB species have different adaptations to salinity (Underwood et al., 1998), and the distribution can be mainly explained by hydrodynamics (Méléder et al., 2007). In our study area, *Paralia sulcata*, *Cyclotella striata*, *Cyclotella stylorum*, *Actinoptychus undulatus*, *Thalassiosira weissflogii*, *Nitzschia cocconeiformis* and *Rhaphoneis amphiceros* are positively correlated with salinity (Sun, 2022). In addition, *Paralia sulcata* was the most dominant species in the northern area. As an epipelic diatom, it can secrete large quantities of EPS (Underwood and Paterson, 2003), which can further promote sediment stability (Kim et al., 2021) in the northern region.

Furthermore, photosynthetic efficiency could be another factor governing seasonal variation of MPB biomass. Summer temperatures and irradiance are high in the study area. Sun (2022) showed that the dominant species here has a wide temperature tolerance range. This suggests that thermo-induced inhibition of photosynthesis did not play a significant role here. For other temperate tidal flats with an opposite

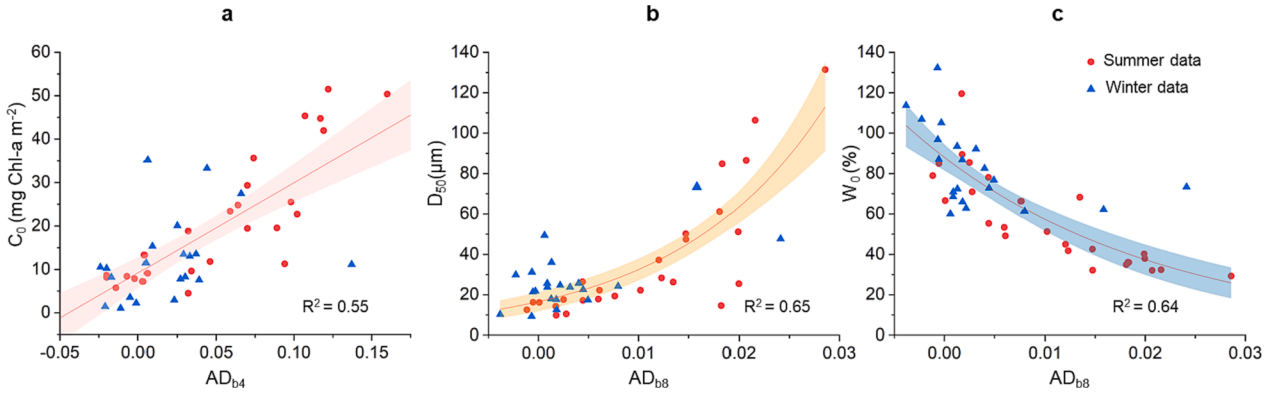


**Fig. 7.** Best regression models for a) surface biomass ($C_0$), b) sediment grain-size ($D_{50}$) and c) water content ($W_0$) based on the in-situ data. The in-situ spectral data were resampled to the spectral reflectance of Sentinel 2. The absorption depth of band 4 ($AD(b_4)$) and absorption depth of band 8 ($(AD(b_8)$) are the input parameter for these models. The shaded area is a 95% confidence interval.

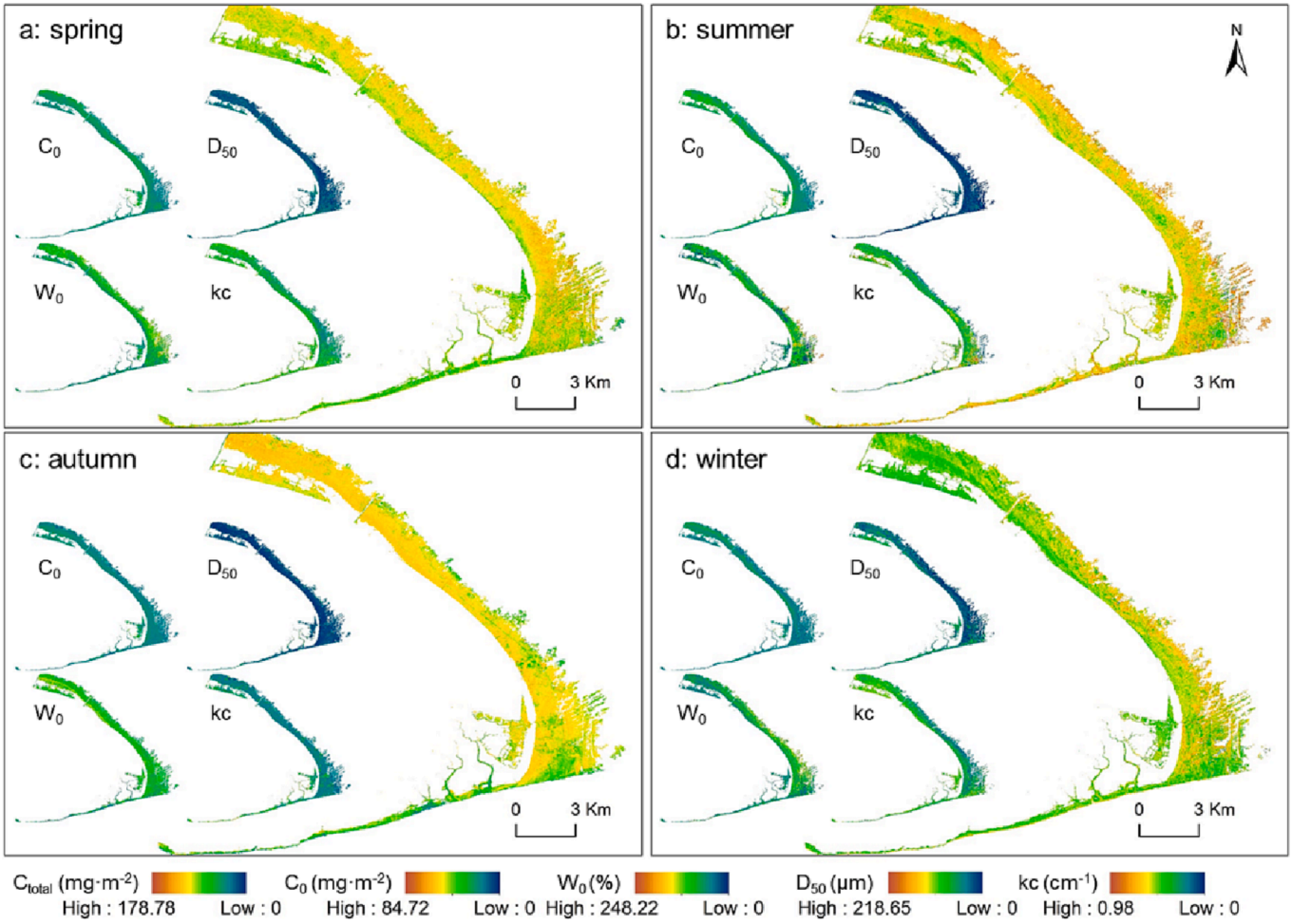


**Fig. 8.** Seasonal distribution map of total biomass, including spring (a), summer (b), autumn (c), and winter (d). The small figures inside are $C_0$ (upper left), $D_{50}$ (upper right), $W_0$ (lower left), and kc (lower right), based on seasonal composites of satellite data from March 2020 to February 2021.

seasonal trend at the sediment surface, thermo-inhibition combined with grazing pressure and algal dynamics are considered to be the reason for the MPB biomass decrease in summer (Kwon et al., 2016; Savelli et al., 2018). In addition, a different seasonal distribution of surface MPB biomass between northern and southern European tidal flats has been reported (Brito et al., 2010; Haro et al., 2020). Comprehensive observations of the spatiotemporal distribution patterns of MPB on tidal flats across the globe may help to unravel the mechanisms of MPB variation.

### 4.2. *Sentinel satellite data capabilities for total biomass mapping*

Remote sensing is an efficient and repeatable method for obtaining a total MPB biomass map at a non-microscopic scale (>1 cm) in both horizontal and vertical directions through measured data. Unlike most studies focusing on the superficial zone (Daggers et al., 2018; Haro et al., 2020), this study tests the validity of the exponential decay model and expands the scale of the remote sensing application of MPB. It can further help evaluate the ecological functions of MPB and optimise management. For example, in terms of energy transfer, there are strong trophic cascade effects between the MPB, invertebrates and shorebirds, which are not limited to the surface of tidal flats (Elner et al., 2005; Herman et al., 2000; van Gils et al., 2016). Our satellite-derived total MPB biomass maps can help to conduct dynamic habitat management for organisms on the tidal flat. Oakes and Eyre (2014) found that MPB and bacteria in sandy mud together accounted for 89% of the organic carbon in the surface sediment layer (0–2 cm) and 77% in the deeper layer (2–5 cm). Hence, remote sensing, combined with modelling, can fill a niche in large-area total biomass mapping and assessment of ecosystem functioning.

The construction of an algorithm of the depth decay rate based on the sediment properties $C_0$, $D_{50}$ and $W_0$ and making it mappable are other contributions of this study. Although MPB mapping poses challenges due to spectral similarity with other ground features (Tebbs et al., 2015), many methods have successfully mapped surface MPB biomass $C_0$ in tidal systems worldwide, including the Tagus Estuary (Brito et al., 2013), Westerschelde Estuary (Daggers et al., 2020a), the Ems Estuary (Jacobs et al., 2021), and inner Cadiz Bay (Haro et al., 2022), etc. The estimation of $D_{50}$ and $W_0$ has also been the focus of attention (e.g. Kim et al., 2019; Madhuanand et al., 2023; Rainey et al., 2003). Our study found that NIR is sensitive to the sediment background, which is consistent with previous studies. Combe et al. (2005) suggested that MPB biofilms have a 100% transmittance spectral window in 750–920 nm and can obtain the optical properties of the background. Numerous studies have demonstrated that the spectral response of water is sensitive in the NIR, and water significantly decreases sediment average brightness or albedo (Barillé et al., 2011; Xu, 2006). Verpoorter et al. (2014) suggested that grain size variations influence the overall shape of the spectrum at 350–2500 nm and that considering the sediment grain size is necessary for water content estimation. In this study, the features of $D_{50}$ and $W_0$ overlapped in the NIR band; an absorption feature of water at 980 nm was acquired when the water content was 70%, which was also mentioned in the study by Launeau et al.(2018). Our algorithm utilized the NIR band (Band 8) of Sentinel-2, which within the range of

400–900 nm, thereby avoiding the potential deviations resulting from water absorption at 980 nm. However, to further enhance its performance, the algorithm could also incorporate features from shortwave infrared band(s).

Furthermore, it is worth mentioning that the overestimation of biomass $C_0$ (Fig. S4a) and $D_{50}$ (Fig. S4b) may result from the sampling strategy, and scale conversion between ground spectral measurement and remote sensing application. Especially crab burrows on the tidal flat in the study area will increase spectral absorption at larger spatial scale, leading to overestimation (Zhang et al., 2021). Underestimation of $W_0$ may result from the tidal level influence because the satellite data used for validation were collected at the lowest tide, while the in-situ data were collected 1–2 h before and after transit of the satellite.

### 4.3. Limitations and opportunities

The distribution of MPB biomass is a function of environmental and biological variables and feedbacks (i.e., tides, hydrodynamics, sediment microtopography, sediment porosity and cohesivity, nutrients, light, temperature, predation, nutrient uptake, growth and mortality, and migration) (Kromkamp et al., 2006), as well as e.g., bioturbation by fauna. This is very similar to the factors influencing the distribution of phytoplankton, which is another essential source of primary productivity of the estuarine tidal flats and is typically studied using a combination of field investigation, satellite, modeling, and modern autonomous technologies (Ardyna et al., 2020). However, autonomous technologies, such as unmanned sampling, were not used in this study. Combining such technology with a refined sampling strategy (e.g., 0.1 mm vertical layers) may enhance the vertical data collection, assist in collecting samples from a larger area and improve the efficiency of calibration or validation for monitoring total biomass. Although our results confirmed the exponentially-decreasing gradient of chlorophyll with depth found in previous studies that used cryo-slicing (e.g. Kromkamp et al., 2006), a more multidisciplinary approach should be considered to explore the mechanisms of MPB biomass decay, improving the formulation of the decay rate based on physical principles.

Moreover, although the control experiments helped to find sensitive bands for estimating $D_{50}$ and $W_0$, efforts are still needed to improve this part. First, we used the loss on ignition method (set at 550 °C) to remove organic matter. This method removed not only organic matter (consisting of carbon and nutrients in the form of carbohydrates, proteins, fats and nucleic acids), which ignited between 384 and 563 °C, but also core water and probably even changed the grain size, as temperatures between 100 and 380 °C could result in mineral dehydration (Bensharada et al., 2022). In addition, burning sediment can alter the optical properties, which can be visually seen from the colour. After removing organic matter, the red band's spectral change rate changed more than the blue and green bands (Fig. 7), and sediments with smaller median grain sizes were redder (Fig. 3). Therefore, the comparison of the two sediment groups with and without organic matter removal did not strictly control for other conditions. Second, we removed Chl-a by natural degradation effectively as the obtained spectral curve has almost no absorption in the red band (Fig. 5), while the applicability of the results will improve if the MPB biomass in sediment can be controlled. Third, although the range of $D_{50}$ among the control experiment tried to cover the overall level of the Changjiang estuary, the mean value of $D_{50}$ in the Changjiang estuary is lower than that in other estuarine tidal flats, such as the Westerschelde estuary in the Netherlands, the Humber estuary in the UK (Hu et al., 2021), Hanko Peninsula in Finland (Gammal et al., 2019), and the Authie estuary in France (Verpoorter et al., 2020). Hence, a more extensive $D_{50}$ range can help to conclude that it is more widely used. We highlight the need for more elaborate experiments to explore the spectral interaction between TOC and other parameters under different physicochemical states. We recommend further independent validation to evaluate the performance of the algorithms in different seasons. In addition, we recommend calibration and validation of the algorithms when used in other tidal flats.

## 5. Conclusions

Combined with in-situ data, our approach showed the potential for large-scale total MPB biomass estimation using remotely sensed surface variables, including surface MPB ($C_0$), sediment median grain-size ($D_{50}$) and water content ($W_0$). It also provides an understanding of the spectral response under controllable conditions, showing that the NIR band was sensitive to the variations in $D_{50}$ and $W_0$. Moreover, the exponential decay model for quantifying the MPB vertical distribution was validated for our study area at Chongming Dongtan, and the estimated scale was extended by making the decay rate kc mappable using satellite data.

## CRediT authorship contribution statement

**Ting Zhang:** Conceptualization, Methodology, Formal analysis, Writing – original draft. **Bo Tian:** Writing – review & editing, Funding acquisition. **Yujue Wang:** Resources, Investigation. **Dongyan Liu:** Resources. **Yunxuan Zhou:** Writing – review & editing, Funding acquisition, Supervision. **Daphne van der Wal:** Conceptualization, Writing – review & editing, Supervision.

## Declaration of Competing Interest

The authors declare that they have no known competing financial interests or personal relationships that could have appeared to influence the work reported in this paper.

## Data availability

The data that support the findings of this study will be openly available in the 4TU.Research Data repository after acceptance.

## Acknowledgements

This work is supported by the project "Coping with Deltas in Transition" within the Programme for Strategic Scientific Alliances between the People's Republic of China and The Netherlands (PSA) and financed by the Chinese Ministry of Science and Technology (MOST) (grant number 2016YFE0133700), the Royal Netherlands Academy of Arts and Sciences (KNAW) (grant number PSA-SA-E-02); and the CSC scholarship (grant number 202006140100). We would like to thank Ke Ye, Ya Peng, and Wenhao Jiang for assistance of sample collection during field measurement. We acknowledge the support of Chongming Dongtan Nature Reserve for this study. We would also like to thank the anonymous referees for their constructive reviews.

## Appendix A. Supplementary data

Supplementary data to this article can be found online at https://doi.org/10.1016/j.jag.2023.103417.

## References

Ardyna, M., Mundy, C.J., Mayot, N., Matthes, L.C., Oziel, L., Horvat, C., Leu, E., Assmy, P., Hill, V., Matrai, P.A., Gale, M., Melnikov, I.A., Arrigo, K.R., 2020. Under-Ice Phytoplankton Blooms: Shedding Light on the "Invisible" Part of Arctic Primary Production. Front. Mar. Sci. 7, 1–25. https://doi.org/10.3389/fmars.2020.608032.

Barillé, L., Méléder, V., Combe, J.P., Launeau, P., Rincé, Y., Carrère, V., Morançais, M., 2007. Comparative analysis of field and laboratory spectral reflectances of benthic diatoms with a modified Gaussian model approach. J. Exp. Mar. Bio. Ecol. 343, 197–209. https://doi.org/10.1016/j.jembe.2006.11.013.

Barillé, L., Mouget, J.-L., Méléder, V., Rosa, P., Jesus, B., 2011. Spectral response of benthic diatoms with different sediment backgrounds. Remote Sens. Environ. 115, 1034–1042. https://doi.org/10.1016/j.rse.2010.12.008.

Bensharada, M., Telford, R., Stern, B., Gaffney, V., 2022. Loss on ignition vs. thermogravimetric analysis: a comparative study to determine organic matter and

carbonate content in sediments. J. Paleolimnol. 67, 191–197. https://doi.org/10.1007/s10933-021-00209-6.
Benyoucef, I., Blandin, E., Lerouxel, A., Jesus, B., Rosa, P., Méléder, V., Launeau, P., Barillé, L., 2014. Microphytobenthos interannual variations in a north-European estuary (Loire estuary, France) detected by visible-infrared multispectral remote sensing. Estuar. Coast. Shelf Sci. 136, 43–52. https://doi.org/10.1016/j.ecss.2013.11.007.
Brito, A.C., Newton, A., Tett, P., Icely, J., Fernandes, T.F., 2010. The yield of microphytobenthic chlorophyll from nutrients: Enriched experiments in microcosms. J. Exp. Mar. Bio. Ecol. 384, 30–43. https://doi.org/10.1016/j.jembe.2009.11.010.
Brito, A.C., Benyoucef, I., Jesus, B., Brotas, V., Gernez, P., Mendes, C.R., Launeau, P., Dias, M.P., Barillé, L., 2013. Seasonality of microphytobenthos revealed by remote-sensing in a South European estuary. Cont. Shelf Res. 66, 83–91. https://doi.org/10.1016/j.csr.2013.07.004.
Brotas, V., Serôdio, J., 1995. A mathematical model for the vertical distribution of chlorophyllA in estuarine intertidal sediments. Netherlands J. Aquat. Ecol. 29, 315–321. https://doi.org/10.1007/BF02084230.
Cahoon, L.B., 1999. The role of benthic microalgae in neritic ecosystems. In: Ansell, A., Gibson, R.N., Barnes, M. (Eds.), OceAnography And Marine Biology, An Annual Review. CRC Press, p. 40. https://doi.org/10.1201/9781482298550.
Coelho, H., Vieira, S., Serôdio, J., 2009. Effects of desiccation on the photosynthetic activity of intertidal microphytobenthos biofilms as studied by optical methods. J. Exp. Mar. Bio. Ecol. 381, 98–104. https://doi.org/10.1016/j.jembe.2009.09.013.
Combe, J., Launeau, P., Carrere, V., Despan, D., Meleder, V., Barille, L., Sotin, C., 2005. Mapping microphytobenthos biomass by non-linear inversion of visible-infrared hyperspectral images. Remote Sens. Environ. 98, 371–387. https://doi.org/10.1016/j.rse.2005.07.010.
Daggers, T.D., Kromkamp, J.C., Herman, P.M.J., van der Wal, D., 2018. A model to assess microphytobenthic primary production in tidal systems using satellite remote sensing. Remote Sens. Environ. 211, 129–145. https://doi.org/10.1016/j.rse.2018.03.037.
Daggers, T.D., Herman, P.M.J., van der Wal, D., 2020a. Seasonal and Spatial Variability in Patchiness of Microphytobenthos on Intertidal Flats From Sentinel-2 Satellite Imagery. Front. Mar. Sci. 7, 1–14. https://doi.org/10.3389/fmars.2020.00392.
Daggers, T.D., Oevelen, D., Herman, P.M.J., Boschker, H.T.S., Wal, D., 2020b. Spatial variability in macrofaunal diet composition and grazing pressure on microphytobenthos in intertidal areas. Limnol. Oceanogr. 65, 2819–2834. https://doi.org/10.1002/lno.11554.
de Vet, P.L.M., van Prooijen, B.C., Wang, Z.B., 2017. The differences in morphological development between the intertidal flats of the Eastern and Western Scheldt. Geomorphology 281, 31–42. https://doi.org/10.1016/j.geomorph.2016.12.031.
Du, G.Y., Son, M., An, S., Chung, I.K., 2010. Temporal variation in the vertical distribution of microphytobenthos in intertidal flats of the Nakdong River estuary. Korea. Estuar. Coast. Shelf Sci. 86, 62–70. https://doi.org/10.1016/j.ecss.2009.10.008.
Echappé, C., Gernez, P., Méléder, V., Jesus, B., Cognie, B., Decottignies, P., Sabbe, K., Barillé, L., 2018. Satellite remote sensing reveals a positive impact of living oyster reefs on microalgal biofilm development. Biogeosciences 15, 905–918. https://doi.org/10.5194/bg-15-905-2018.
Elner, R.W., Beninger, P.G., Jackson, D.L., Potter, T.M., 2005. Evidence of a new feeding mode in western sandpiper (Calidris mauri) and dunlin (Calidris alpina) based on bill and tongue morphology and ultrastructure. Mar. Biol. 146, 1223–1234. https://doi.org/10.1007/s00227-004-1521-5.
ESA, 2015. Sentinel-2 User Handbook. 10.13128/REA-22658.
Frankenbach, S., Azevedo, A.A., Reis, V., Dias, D., Vaz, L., Dias, J.M., Serôdio, J., 2019. Functional resilience of PSII, vertical distribution and ecosystem-level estimates of subsurface microphytobenthos in estuarine tidal flats. Cont. Shelf Res. 182, 46–56. https://doi.org/10.1016/j.csr.2019.05.018.
Gammal, J., Järnström, M., Bernard, G., Norkko, J., Norkko, A., 2019. Environmental Context Mediates Biodiversity-Ecosystem Functioning Relationships in Coastal Soft-sediment Habitats. Ecosystems 22, 137–151. https://doi.org/10.1007/s10021-018-0258-9.
Haro, S., Lara, M., Laiz, I., González, C.J., Bohórquez, J., Garcia-Robledo, E., Corzo, A., Papaspyrou, S., 2020. Microbenthic Net Metabolism Along Intertidal Gradients (Cadiz Bay, SW Spain): Spatio-Temporal Patterns and Environmental Factors. Front. Mar. Sci. 7 https://doi.org/10.3389/fmars.2020.00039.
Haro, S., Jesus, B., Oiry, S., Papaspyrou, S., Lara, M., González, C.J., Corzo, A., 2022. Microphytobenthos spatio-temporal dynamics across an intertidal gradient using Random Forest classification and Sentinel-2 imagery. Sci. Total Environ. 804, 149983 https://doi.org/10.1016/j.scitotenv.2021.149983.
Herman, P., Middelburg, J., Widdows, J., Lucas, C., Heip, C., 2000. Stable isotopes as trophic tracers: combining field sampling and manipulative labelling of food resources for macrobenthos. Mar. Ecol. Prog. Ser. 204, 79–92. https://doi.org/10.3354/meps204079.
Hope, J.A., Paterson, D.M., Thrush, S.F., 2020. The role of microphytobenthos in soft-sediment ecological networks and their contribution to the delivery of multiple ecosystem services. J. Ecol. 108, 815–830. https://doi.org/10.1111/1365-2745.13322.
Hu, Z., Willemsen, P.W.J.M., Borsje, B.W., Wang, C., Wang, H., Van Der Wal, D., Zhu, Z., Oteman, B., Vuik, V., Evans, B., Möller, I., Belliard, J.P., Van Braeckel, A., Temmerman, S., Bouma, T.J., 2021. Synchronized high-resolution bed-level change and biophysical data from 10 marsh-mudflat sites in northwestern Europe. Earth Syst. Sci. Data 13, 405–416. https://doi.org/10.5194/essd-13-405-2021.
Jacobs, P., Pitarch, J., Kromkamp, J.C., Philippart, C.J.M., 2021. Assessing biomass and primary production of microphytobenthos in depositional coastal systems using spectral information. PLoS One 16, e0246012.
Jesus, B., Mendes, C.R., Brotas, V., Paterson, D.M., 2006. Effect of sediment type on microphytobenthos vertical distribution: Modelling the productive biomass and improving ground truth measurements. J. Exp. Mar. Bio. Ecol. 332, 60–74. https://doi.org/10.1016/j.jembe.2005.11.005.
Kazemipour, F., Launeau, P., Méléder, V., 2012. Microphytobenthos biomass mapping using the optical model of diatom biofilms: Application to hyperspectral images of Bourgneuf Bay. Remote Sens. Environ. 127, 1–13. https://doi.org/10.1016/j.rse.2012.08.016.
Kim, K.-L., Kim, B.-J., Lee, Y.-K., Ryu, J.-H., 2019. Generation of a Large-Scale Surface Sediment Classification Map using Unmanned Aerial Vehicle (UAV) Data: A Case Study at the Hwang-do Tidal Flat. Korea. Remote Sens. 11, 229. https://doi.org/10.3390/rs11030229.
Kim, B., Lee, J., Noh, J., Bae, H., Lee, C., Ha, H.J., Hwang, K., Kim, D.-U., Kwon, B.-O., Ha, H.K., Pierre, G., Delattre, C., Michaud, P., Khim, J.S., 2021. Spatiotemporal variation of extracellular polymeric substances (EPS) associated with the microphytobenthos of tidal flats in the Yellow Sea. Mar. Pollut. Bull. 171, 112780 https://doi.org/10.1016/j.marpolbul.2021.112780.
Kromkamp, J.C., Brouwer, J.F.C. de, Blanchard, G.F., Forster, R.M., Créach, V., 2006. Functioning of microphytobenthos in estuaries, Royal Netherlands Academy of Arts and Sciences. Amsterdam. 10.1016/0165-2478(89)90061-8.
Kromkamp, J.C., Morris, E., Forster, R.M., 2020. Microscale Variability in Biomass and Photosynthetic Activity of Microphytobenthos During a Spring-Neap Tidal Cycle. Front. Mar. Sci. 7, 1–15. https://doi.org/10.3389/fmars.2020.00562.
Kwon, B.-O., Lee, Y., Park, J., Ryu, J., Hong, S., Son, S., Lee, S.Y., Nam, J., Koh, C.-H., Khim, J.S., 2016. Temporal dynamics and spatial heterogeneity of microalgal biomass in recently reclaimed intertidal flats of the Saemangeum area. Korea. J. Sea Res. 116, 1–11. https://doi.org/10.1016/j.seares.2016.08.002.
Lambe, T.W., Whitman, R.V., 1991. Soil Mechanics. John Wiley & Sons, p. 576.
Launeau, P., Méléder, V., Verpoorter, C., Barillé, L., Kazemipour-Ricci, F., Giraud, M., Jesus, B., Le Menn, E., 2018. Microphytobenthos Biomass and Diversity Mapping at Different Spatial Scales with a Hyperspectral Optical Model. Remote Sens. 10, 716. https://doi.org/10.3390/rs10050716.
Li, X., Zhou, Y., Zhang, L., Kuang, R., 2014. Shoreline change of Chongming Dongtan and response to river sediment load: A remote sensing assessment. J. Hydrol. 511, 432–442. https://doi.org/10.1016/j.jhydrol.2014.02.013.
Lichtenberg, M., Cartaxana, P., Kühl, M., 2020. Vertical Migration Optimizes Photosynthetic Efficiency of Motile Cyanobacteria in a Coastal Microbial Mat. Front. Mar. Sci. 7 https://doi.org/10.3389/fmars.2020.00359.
Liu, W., Zhang, J., Tian, G., Xu, H., Yan, X., 2013. Temporal and vertical distribution of microphytobenthos biomass in mangrove sediments of Zhujiang (Pearl River) Estuary. Acta Oceanol. Sin. 32, 82–88. https://doi.org/10.1007/s13131-013-0302-8.
MacIntyre, H.L., Geider, R.J., Miller, D.C., 1996. Microphytobenthos: The Ecological Role of the "Secret Garden" of Unvegetated, Shallow-Water Marine Habitats. I. Distribution, Abundance and Primary Production. Estuaries 19, 186. https://doi.org/10.2307/1352224.
Madhuanand, L., Philippart, C.J.M., Wang, J., Nijland, W., de Jong, S.M., Bijleveld, A.I., Addink, E.A., 2023. Enhancing the predictive performance of remote sensing for ecological variables of tidal flats using encoded features from a deep learning model. GIScience Remote Sens. 60 https://doi.org/10.1080/15481603.2022.2163048.
Méléder, V., Barillé, L., Launeau, P., Carrère, V., Rincé, Y., 2003a. Spectrometric constraint in analysis of benthic diatom biomass using monospecific cultures. Remote Sens. Environ. 88, 386–400. https://doi.org/10.1016/j.rse.2003.08.009.
Méléder, V., Launeau, P., Barillé, L., Rincé, Y., 2003b. Cartographie des peuplements du microphytobenthos par télédétection spatiale visible-infrarouge dans un écosystème conchylicole. C. R. Biol. 326, 377–389. https://doi.org/10.1016/S1631-0691(03)00125-2.
Méléder, V., Rincé, Y., Barillé, L., Gaudin, P., Rosa, P., 2007. Spatiotemporal changes in microphytobenthos assemblages in a macrotidal flat (Bourgneuf Bay, France) 1. J. Phycol. 43, 1177–1190. https://doi.org/10.1111/j.1529-8817.2007.00423.x.
Méléder, V., Savelli, R., Barnett, A., Polsenaere, P., Gernez, P., Cugier, P., Lerouxel, A., Le Bris, A., Dupuy, C., Le Fouest, V., Lavaud, J., 2020. Mapping the Intertidal Microphytobenthos Gross Primary Production Part I: Coupling Multispectral Remote Sensing and Physical Modeling. Front. Mar. Sci. 7 https://doi.org/10.3389/fmars.2020.00520.
Middelburg, J.J., Barranguet, C., Boschker, H.T.S., Herman, P.M.J., Moens, T., Heip, C.H.R., 2000. The fate of intertidal microphytobenthos carbon: An in situ 13 C-labeling study. Limnol. Oceanogr. 45, 1224–1234. https://doi.org/10.4319/lo.2000.45.6.1224.
Miller, D.C., Geider, R.J., MacIntyre, H.L., 1996. Microphytobenthos: The Ecological Role of the "Secret Garden" of Unvegetated, Shallow-Water Marine Habitats. II. Role in Sediment Stability and Shallow-Water Food Webs. Estuaries 19, 202. https://doi.org/10.2307/1352225.
Ming-Yi, S., Lee, C., Aller, R.C., 1993. Laboratory studies of oxic and anoxic degradation of chlorophyll-a in Long Island Sound sediments. Geochim. Cosmochim. Acta 57, 147–157. https://doi.org/10.1016/0016-7037(93)90475-C.
Montserrat, F., Van Colen, C., Degraer, S., Ysebaert, T., Herman, P., 2008. Benthic community-mediated sediment dynamics. Mar. Ecol. Prog. Ser. 372, 43–59. https://doi.org/10.3354/meps07769.
Montserrat, F., Van Colen, C., Provoost, P., Milla, M., Ponti, M., Van den Meersche, K., Ysebaert, T., Herman, P.M.J., 2009. Sediment segregation by biodiffusing bivalves. Estuar. Coast. Shelf Sci. 83, 379–391. https://doi.org/10.1016/j.ecss.2009.04.010.
Moore, A.W., Lee, M.S., 1994. Efficient Algorithms for Minimizing Cross Validation Error, in: Machine Learning Proceedings 1994. Elsevier, pp. 190–198. 10.1016/B978-1-55860-335-6.50031-3.

Murphy, R.J., Underwood, A.J., Tolhurst, T.J., Chapman, M.G., 2008. Field-based remote-sensing for experimental intertidal ecology: Case studies using hyperspatial and hyperspectral data for New South Wales (Australia). Remote Sens. Environ. 112, 3353–3365. https://doi.org/10.1016/j.rse.2007.09.016.

Murray, N.J., Phinn, S.R., DeWitt, M., Ferrari, R., Johnston, R., Lyons, M.B., Clinton, N., Thau, D., Fuller, R.A., 2019. The global distribution and trajectory of tidal flats. Nature 565, 222–225. https://doi.org/10.1038/s41586-018-0805-8.

Oakes, J.M., Eyre, B.D., 2014. Transformation and fate of microphytobenthos carbon in subtropical, intertidal sediments: Potential for long-term carbon retention revealed by 13C-labeling. Biogeosciences 11, 1927–1940. https://doi.org/10.5194/bg-11-1927-2014.

Otsu, N., 1979. A Threshold Selection Method from Gray-Level Histograms. IEEE Trans. Syst. Man. Cybern. 9, 62–66. https://doi.org/10.1109/TSMC.1979.4310076.

Paterson, D.M., Hagerthey, S.E., 2001. Microphytobenthos in Constrasting Coastal Ecosystems: Biology and Dynamics. pp. 105–125. 10.1007/978-3-642-56557-1_6.

Rainey, M., Tyler, A., Gilvear, D., Bryant, R., McDonald, P., 2003. Mapping intertidal estuarine sediment grain size distributions through airborne remote sensing. Remote Sens. Environ. 86, 480–490. https://doi.org/10.1016/S0034-4257(03)00126-3.

Ratkowsky, D.A., 1990. Handbook of Nonlinear Regression Models (Statistics, A Series of Textbooks and Monographs).

Riaux-Gobin, C., Llewellyn, C., Klein, B., 1987. Microphytobenthos from two subtidal sediments from North Brittany. II. Variations of pigment compositions and concentrations determinded by HPLC and conventional techniques. Mar. Ecol. Prog. Ser. 40, 275–283. https://doi.org/10.3354/meps040275.

Riekenberg, P.M., Oakes, J.M., Eyre, B.D., 2020. A shift in the pool of retained microphytobenthos nitrogen under enhanced nutrient availability. Water Res. 187, 116438 https://doi.org/10.1016/j.watres.2020.116438.

Savelli, R., Dupuy, C., Barillé, L., Lerouxel, A., Guizien, K., Philippe, A., Bocher, P., Polsenaere, P., Le Fouest, V., 2018. On biotic and abiotic drivers of the microphytobenthos seasonal cycle in a temperate intertidal mudflat: A modelling study. Biogeosciences 15, 7243–7271. https://doi.org/10.5194/bg-15-7243-2018.

Schwarz, G., 1978. Estimating the Dimension of a Model. Inst. Math. Stat. 6, 461–464. stable/2958889.

Serôdio, J., Coelho, H., Vieira, S., Cruz, S., 2006. Microphytobenthos vertical migratory photoresponse as characterised by light-response curves of surface biomass. Estuar. Coast. Shelf Sci. 68, 547–556. https://doi.org/10.1016/j.ecss.2006.03.005.

Strickland, J.D.H., Parsons, T.R., 1972. A Practical Handbook of Seawater Analysis, 2nd edition. Fisheries Research Board of Canada, Ottawa, Canada. 10.25607/OBP-1791.

Sun, S., 2022. Study on the benthic diatom communities and its contributions to the food web in the Chongming Dongtan mudflats. East China Normal University.

Tebbs, E.J., Remedios, J.J., Avery, S.T., Rowland, C.S., Harper, D.M., 2015. Regional assessment of lake ecological states using Landsat: A classification scheme for alkaline–saline, flamingo lakes in the East African Rift Valley. Int. J. Appl. Earth Obs. Geoinf. 40, 100–108. https://doi.org/10.1016/j.jag.2015.03.010.

Underwood, G.J.C., Kromkamp, J., 1999. Primary Production by Phytoplankton and Microphytobenthos in Estuaries. pp. 93–153. 10.1016/S0065-2504(08)60192-0.

Underwood, G.J.C., Paterson, D.M., 2003. The importance of extracellular carbohydrate productionby marine epipelic diatoms. Adv. Bot. Res. https://doi.org/10.1016/S0065-2296(05)40005-1.

Underwood, G., Phillips, J., Saunders, K., 1998. Distribution of estuarine benthic diatom species along salinity and nutrient gradients Distribution of estuarine benthic diatom species along salinity and nutrient gradients. Eur. J. Phycol. ISSN 33, 173–183. https://doi.org/10.1080/09670269810001736673.

van der Meer, F., 2004. Analysis of spectral absorption features in hyperspectral imagery. Int. J. Appl. Earth Obs. Geoinf. 5, 55–68. https://doi.org/10.1016/j.jag.2003.09.001.

van der Wal, D., Herman, P., Forster, R., Ysebaert, T., Rossi, F., Knaeps, E., Plancke, Y., Ides, S., 2008. Distribution and dynamics of intertidal macrobenthos predicted from remote sensing: response to microphytobenthos and environment. Mar. Ecol. Prog. Ser. 367, 57–72. https://doi.org/10.3354/meps07535.

van der Wal, D., Wielemaker-van den Dool, A., Herman, P.M.J., 2010. Spatial Synchrony in Intertidal Benthic Algal Biomass in Temperate Coastal and Estuarine Ecosystems. Ecosystems 13, 338–351. https://doi.org/10.1007/s10021-010-9322-9.

van Gils, J.A., Lisovski, S., Lok, T., Meissner, W., Ozarowska, A., de Fouw, J., Rakhimberdiev, E., Soloviev, M.Y., Piersma, T., Klaassen, M., 2016. Body shrinkage due to Arctic warming reduces red knot fitness in tropical wintering range. Science (80-.) 352, 819–821. https://doi.org/10.1126/science.aad6351.

Verpoorter, C., Carrère, V., Combe, J.-P., 2014. Visible, near-infrared spectrometry for simultaneous assessment of geophysical sediment properties (water and grain size) using the Spectral Derivative-Modified Gaussian Model. J. Geophys. Res. Earth Surf. 119, 2098–2122. https://doi.org/10.1002/2013JF002969.

Verpoorter, C., Menuge, B., Launeau, P., Méléder, V., Héquette, A., Cartier, A., Sipka, V., 2020. Synergy Between Hyperspectral (HYSPEX), Multispectral (SPOT 6/7, Sentinel-2) Remotely Sensed Data and LiDAR Data for Mapping the Authie Estuary (France). pp. 769–788. 10.1007/978-981-15-2081-5_45.

Wang, X., Sun, J., Zhao, Z., 2020. Effects of river discharge and tidal meandering on morphological changes in a meso tidal creek. Estuar. Coast. Shelf Sci. 234, 106635 https://doi.org/10.1016/j.ecss.2020.106635.

Wei, J., Wang, M., Jiang, L., Yu, X., Mikelsons, K., Shen, F., 2021. Global Estimation of Suspended Particulate Matter From Satellite Ocean Color Imagery. J. Geophys. Res. Ocean. 126 https://doi.org/10.1029/2021JC017303.

Xu, H., 2006. Modification of normalised difference water index (NDWI) to enhance open water features in remotely sensed imagery. Int. J. Remote Sens. 27, 3025–3033. https://doi.org/10.1080/01431160600589179.

Yin, K., Zetsche, E.M., Harrison, P.J., 2016. Effects of sandy vs muddy sediments on the vertical distribution of microphytobenthos in intertidal flats of the Fraser River Estuary. Canada. Environ. Sci. Pollut. Res. 23, 14196–14209. https://doi.org/10.1007/s11356-016-6571-y.

Zhang, T., Tian, B., Bo, S., Yuan, L., Zhao, Y., Yuan, X., 2018. Mapping the conservation priority of migratory shorebird habitat on a dynamic deltaic coast. Estuar. Coast. Shelf Sci. 212, 219–232. https://doi.org/10.1016/j.ecss.2018.07.010.

Zhang, T., Tian, B., Wang, Y., Liu, D., Sun, S., Duan, Y., Zhou, Y., 2021. Quantifying seasonal variations in microphytobenthos biomass on estuarine tidal flats using Sentinel-1/2 data. Sci. Total Environ. 777, 146051 https://doi.org/10.1016/j.scitotenv.2021.146051.